Check for updates

ADVANCED MATERIALS
www.advmat.de

Rational Molecular Design of π-Extended Thiazolothiazole for High-Performance UV-OPDs Seamlessly Integrated with CMOS

Jaehee Park, Won Jun Pyo, Jubin Kang, Taek Min Kim, Sangjun Lee, Jungmin Oh, Seyeon Baek, Seong-Jin Kim, In Hwan Jung, and Dae Sung Chung**

Vacuum-deposited organic photodiodes (OPDs) offer unique advantages—including narrowband selectivity and compatibility with standard fabrication processes—but achieving ultraviolet (UV) selectivity in such devices remains a key challenge. This is due to the need to reconcile two competing design requirements: 1) strong π–π stacking for efficient charge transport, and 2) limited π-conjugation to retain a wide bandgap suitable for UV absorption and vacuum deposition. Here, we report a molecular design strategy for UV-selective OPDs based on thiazolothiazole (Tz)-based small molecules with tailored backbone planarity and conjugation length. The resulting vacuum-deposited active layers simultaneously exhibit wide bandgaps and robust π–π interactions. The optimized devices achieve outstanding UV selectivity (full-width at half-maximum: 60 nm), high specific detectivity (1.06×10^{12} Jones), and fast dynamic response (cutoff frequency of 50,100 Hz)—representing the highest performance for vacuum-deposited UV-OPDs reported to date. Furthermore, it is demonstrated the seamless integration of these semi-transparent OPDs with complementary metal-oxide-semiconductor (CMOS) image sensors (CIS), underscoring their potential for multifunctional imaging applications. The findings provide key molecular insights for advancing UV-selective organic photodetectors.

1. Introduction

Ultraviolet (UV) radiation is an essential yet potentially harmful component of the solar spectrum, significantly impacting both human health and environmental systems.[1–5] Notably, a 1% depletion in the ozone layer results in ≈2% increase in surface-level UV radiation.[6–8] As UV exposure continues to rise, there is growing demand for sensitive and selective UV detection technologies.

Currently, UV photodetectors are employed in diverse applications such as flame detection, lithography, missile defense, protein analysis, and ozone monitoring.[9–12] In particular, semi-transparent photodetectors that can be seamlessly integrated with commercial complementary metal-oxide-semiconductor (CMOS) image sensors (CIS) have garnered significant interest, as they enable multifunctional imaging without compromising spatial resolution.[13–17] To address these requirements, UV-selective and visible-transparent organic photodiodes (UV-OPDs) have emerged as a compelling alternative to conventional inorganic UV detectors.[18,19] Their intrinsic narrowband UV absorption and high visible transparency—achieved without the need for color filters—make them highly suitable for next-generation optoelectronic platforms.

From a commercialization perspective, vacuum-deposited OPDs are particularly attractive, as they enable large-area fabrication using mature manufacturing infrastructure developed for OLEDs. Nevertheless, most UV-OPDs reported to date rely on the photomultiplication (PM) mechanism, which, while capable of delivering extremely high external quantum efficiencies (EQEs), suffers from inherent limitations such as slow response speeds and high dark currents. For instance, Esopi *et al.* demonstrated solution-processed PM-type UV-OPDs with an EQE of 5,600% and responsivity of 15.9 A W^{-1} at −40 V; however, the devices exhibited response times exceeding 1 s and dark currents over 0.1 mA cm^{-2}.[20] Guo *et al.* reported vacuum-processed PM-type devices with strong UV selectivity and a specific detectivity of 1.28×10^{14} Jones, yet they shared similar drawbacks.[21] Thus, developing high-performance UV-OPDs that simultaneously deliver high UV selectivity, low dark current, and fast dynamic response

J. Park, I. H. Jung
Department of Organic and Nano Engineering
and Human-Tech Convergence Program
Hanyang University
222 Wangsimni-ro, Seongdong-gu, Seoul 04763, Republic of Korea
E-mail: inhjung@hanyang.ac.kr

W. J. Pyo, T. M. Kim, S. Lee, S. Baek, D. S. Chung
Department of Chemical Engineering
Pohang University of Science and Technology (POSTECH)
Pohang 37673, Republic of Korea
E-mail: dchung@postech.ac.kr

J. Kang
Department of Electrical Engineering
Ulsan National Institute of Science and Technology (UNIST)
Ulsan 44919, Republic of Korea

J. Kang, J. Oh, S.-J. Kim
Department of System Semiconductor Engineering
Sogang University
Mapo-gu, Seoul 04107, Republic of Korea

The ORCID identification number(s) for the author(s) of this article can be found under https://doi.org/10.1002/adma.202506449

DOI: 10.1002/adma.202506449

 © 2025 Wiley-VCH GmbH

remains an unresolved challenge—particularly given the conflicting material design requirements of wide bandgaps and strong π–π stacking.

In this study, we synthesized three thiazolothiazole (Tz)-based small molecules via a simple and efficient one-step reaction between an aryl aldehyde and dithiooxamide. Tz is a heteroaromatic ring system composed of two fused thiazole units, offering a π-extended conjugated structure.[22] A key advantage of this synthetic route is its scalability and ease of purification—each compound can be recrystallized to high purity without the need for column chromatography.[23] Tz-based aromatic cores possess highly planar backbones and intrinsic local dipole moments, promoting strong intermolecular π–π stacking and facilitating efficient charge transport in the solid state.[24] Although Tz-based structures have been widely employed in conjugated polymers for organic electronic devices such as solar cells and transistors [25–29] their application in vacuum-deposited OPDs remains largely unexplored.[30] To tune backbone planarity, we designed three Tz-based small molecules by attaching benzene (TzB), α-naphthalene (TzNα), or β-naphthalene (TzNβ) rings symmetrically at both ends of the Tz core. All three compounds exhibited narrow UV absorption within the 300–400 nm range, with distinct differences in molecular planarity. Corresponding UV-OPDs based on TzB, TzNα, and TzNβ showed ultra-narrowband spectral responses, achieving full-width at half-maximum (FWHM) values of 62, 66, and 60 nm, respectively.

Notably, device performance was highly sensitive to the molecular structure. Among the three, TzNβ—with its highly planar and π-extended backbone—delivered the best UV-OPD performance, achieving a responsivity (R) of 38 mA W^{-1} and a specific detectivity (D^*) of 1.06×10^{12} Jones. The TzNβ-based devices also exhibited excellent dynamic response characteristics, with rise times (t_r) and fall times (t_f) of 7.6 and 8.1 µs, respectively, and a –3 dB cutoff frequency of 50,100 Hz. Thanks to their unique combination of high UV selectivity and visible transparency, the OPDs were successfully monolithically integrated onto Si photodiode (Si-PD)-based CIS. The resulting hybrid sensing system demonstrated advanced multifunctional imaging capabilities without spatial loss or resolution degradation caused by crosstalk or optical refraction.

2. Results

2.1. Material Characterization

All UV-selective small molecules were synthesized via a one-step condensation reaction using commercially available precursors: dithiooxamide and three aromatic aldehydes—benzaldehyde, α-naphthaldehyde, and β-naphthaldehyde. Dithiooxamide reacts with the aldehydes to form conjugated thiazolothiazole (Tz)-based small molecules: TzB, TzNα, and TzNβ, respectively. This ring-closing reaction significantly reduces product solubility, enabling straightforward purification through recrystallization by exploiting solubility differences between the products and reactants. When necessary, further purification was carried out via short-column chromatography or vacuum sublimation, enabled by the good solubility of the compounds in chloroform and their low molecular weights. The chemical structures of the synthesized compounds were confirmed by ^{1}H NMR spectroscopy and MALDI-TOF mass spectrometry (Figures S1–S6 (Supporting Information). Synthetic routes for TzB, TzNα, and TzNβ are shown in **Scheme 1**.

The 3D molecular geometries were investigated using B3LYP density functional theory (DFT) calculations with the 6–31G(d,p) basis set (Figures S7 and S8 (Supporting Information). From both top and front views, all three molecules exhibit nearly planar conjugated frameworks. However, side-view analysis reveals distinct differences in backbone planarity. TzB and TzNβ display highly planar structures with near-zero dihedral angles between conjugated units, while TzNα adopts a twisted conformation, with a dihedral angle of ≈32°. This structural distortion is expected to hinder intermolecular stacking and limit charge transport, which may contribute to its comparatively lower OPD performance.

Single-crystal X-ray diffraction (SCXRD) analysis was performed to examine the molecular packing and conformational geometry of TzB, TzNα, and TzNβ. As shown in **Figure 1** and summarized in Table S1 (Supporting Information), TzB adopts a planar backbone with herringbone-type ordering, consistent with the DFT-optimized structure. In contrast, TzNα and TzNβ exhibit larger dihedral angles than those predicted by DFT, with measured twist angles of ≈40° and 20°, respectively, between the Tz core and the terminal aromatic rings. Dihedral angles below 20° are generally favorable for maintaining π-conjugation and promoting intermolecular ordering, while those exceeding 40° tend to hinder both effects.[31] The molecular lengths of TzB and TzNα are ≈12.9 Å, whereas TzNβ extends to 17.3 Å due to its elongated conjugation path. This increased conjugation length is beneficial for enhancing molecular ordering and charge transport within the active layer.[32]

The discrepancy between the DFT-predicted and SCXRD-determined geometries can be attributed to differences in the modeling environment. For TzNβ, the gas-phase DFT calculations predicted a nearly planar structure, while the single-crystal analysis revealed a twist angle of ≈23° due to solid-state intermolecular interactions. While both TzB and TzNβ adopt herringbone-type packing motifs, the nature of their π–π interactions differs significantly. TzB exhibits continuous π–π stacking along its entire backbone, including the thiazole core, with a slightly offset slip-stacked configuration that minimizes electrostatic repulsion and contributes to its high planarity and crystallinity. This uniform stacking consists of both computational and experimental results.

In contrast, TzNβ displays a distinct variation in its stacking arrangement. Although it also adopts a slip-stacked herringbone packing, the molecule features a noticeable twist between the central Tz core and the terminal naphthalene units. As a result, π–π stacking is localized primarily between the terminal naphthalene rings, while the twisted Tz core is excluded from direct intermolecular interactions. This unique packing results in a denser herringbone motif driven by naphthalene-centered interactions.

Thermal stability of the small molecules was evaluated by thermogravimetric analysis (TGA). As shown in Figure S9 (Supporting Information), the 5% weight loss temperatures (T_5%) for TzB, TzNα, and TzNβ were 302, 371, and 394 °C, respectively. The simple benzene end group in TzB offers limited thermal stability, whereas the markedly higher T_5% of TzNβ compared to TzNα

© 2025 Wiley-VCH GmbH

15214095, 2025, 38, Downloaded from https://advanced.onlinelibrary.wiley.com/doi/10.1002/adma.202506449 by Ulsan National Institute Of, Wiley Online Library on [03/12/2025]. See the Terms and Conditions (https://onlinelibrary.wiley.com/terms-and-conditions) on Wiley Online Library for rules of use; OA articles are governed by the applicable Creative Commons License

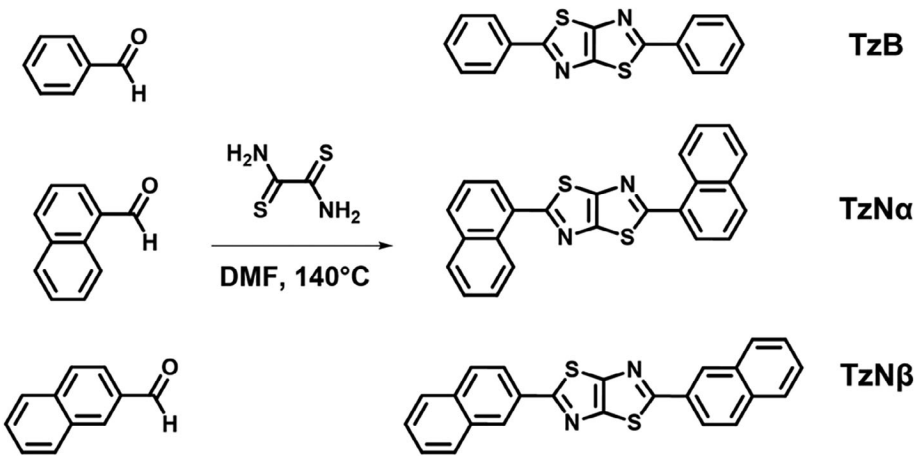

Scheme 1. Synthetic route for TzB, TzNα, and TzNβ via a one-step condensation reaction between aryl aldehydes and dithiooxamide.

suggests that its more planar backbone strengthens the interaction between the Tz and naphthalene moieties. This superior thermal robustness makes TzNβ a more suitable candidate for vacuum thermal evaporation.

The optical absorption properties of the synthesized molecules were measured in chloroform solution (**Figure** 2a). TzB, TzNα, and TzNβ exhibited absorption maxima at 353, 362, and 380 nm, with corresponding full-width at half-maximum (FWHM) values of 55, 72, and 62 nm, respectively. All compounds displayed excellent UV selectivity, as evidenced by their narrow absorption profiles in the 300–400 nm range.

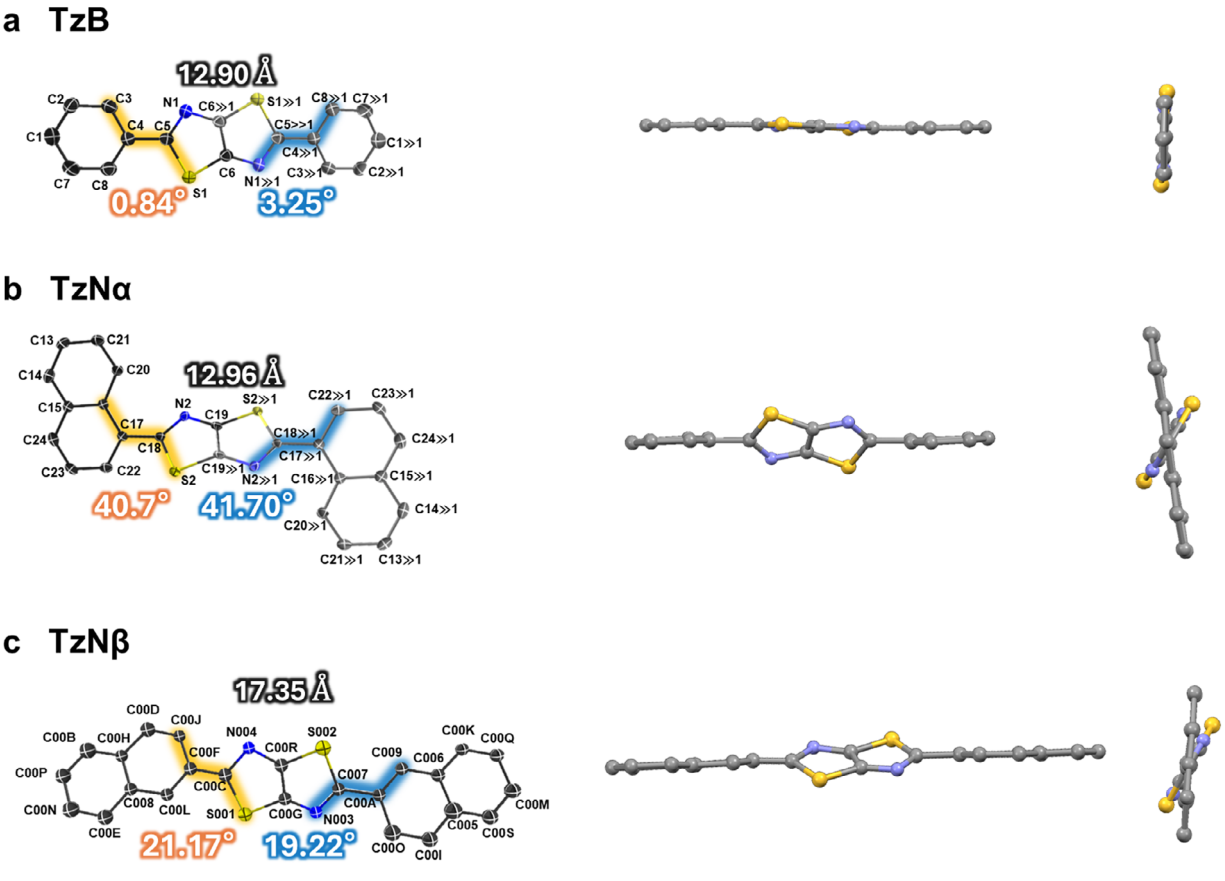

Figure 1. Single-crystal structures of a) TzB, b) TzNα, and c) TzNβ, showing molecular conformations with selected bond lengths (Å) and dihedral angles between the Tz core and terminal aryl groups.

© 2025 Wiley-VCH GmbH

15214095, 2025, 38, Downloaded from https://advanced.onlinelibrary.wiley.com/doi/10.1002/adma.202506449 by Ulsan National Institute Of, Wiley Online Library on [03/12/2025]. See the Terms and Conditions (https://onlinelibrary.wiley.com/terms-and-conditions) on Wiley Online Library for rules of use; OA articles are governed by the applicable Creative Commons License

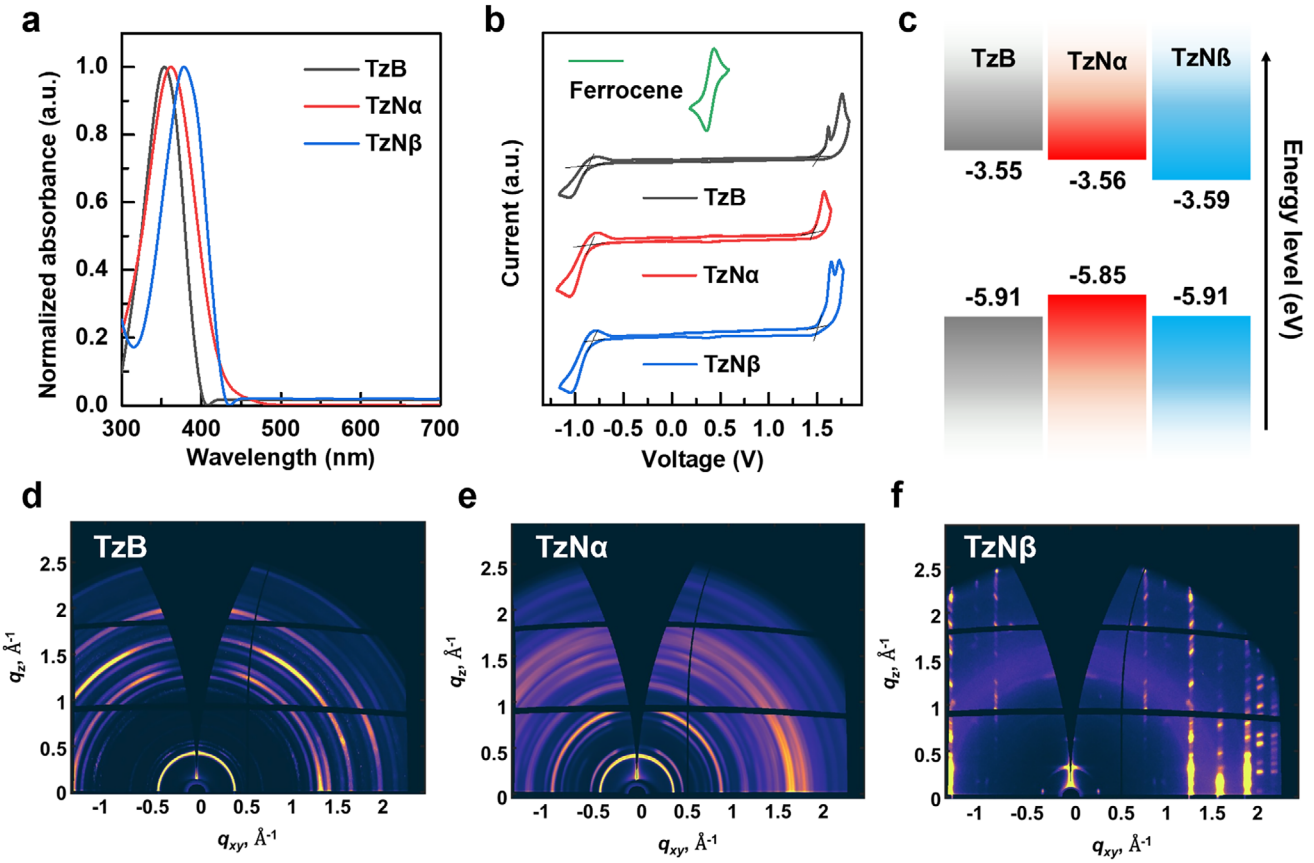

Figure 2. a) UV–vis absorption spectra of TzB, TzNα, and TzNβ measured in chloroform solution. b) Cyclic voltammograms of the three compounds. c) Energy level diagram showing HOMO and LUMO levels estimated from the oxidation and reduction onset potentials in (b). d–f) 2D-GIWAXS patterns of TzB, TzNα, and TzNβ neat films.

The energy levels of the molecules were estimated using cyclic voltammetry (CV) (Figure 2b,c). The highest occupied molecular orbital (HOMO) and lowest unoccupied molecular orbital (LUMO) energy levels were calculated from the oxidation (E_{ox}) and reduction (E_{re}) onset potentials, respectively. The E_{ox} values of TzB, TzNα, and TzNβ were 1.51, 1.45, and 1.51 V, corresponding to HOMO levels of –5.91, –5.85, and –5.91 eV, respectively. Similarly, the E_{re} values were –0.85, –0.84, and –0.81 V, yielding LUMO levels of –3.55, –3.56, and –3.59 eV, respectively.

Among the three, TzB—with the shortest conjugation length—exhibited the largest bandgap. Interestingly, despite their different backbone planarity, TzNα and TzNβ showed similar bandgaps. However, TzNα exhibited upshifted HOMO and LUMO energy levels relative to TzNβ. These results suggest that while backbone planarity has limited influence on the overall bandgap, the specific substitution position on the naphthalene ring (α vs. β) plays a more critical role in determining the absolute energy levels of the small molecules. A summary of the optical and electrochemical properties is provided in **Table 1**.

To examine the morphology of the films, 2D grazing-incidence wide-angle X-ray scattering (2D-GIWAXS) measurements were performed (Figure 2d–f). Although the Tz molecules exhibit

Table 1. Optical and electrochemical properties of TzB, TzNα and TzNβ.

	Optical properties		Electrochemical properties		
	$\lambda_{max,\ sol}$[a] [nm]	$\lambda_{max,\ film}$[b] [nm]	E_{ox}/E_{HOMO}[c] [V/eV]	E_{re}/E_{LUMO}[d] [V/eV]	$E_{g,\ elec}$[e] [eV]
TzB	353	310	1.51 / – 5.91	– 0.85 / –3.55	2.36
TzNα	362	398	1.45 / – 5.85	–0.84 / –3.56	2.29
TzNβ	380	384	1.51 / – 5.91	–0.81 / –3.59	2.32

Maximum absorption peak in (a) solution($\lambda_{max,\ sol}$) and (b) film states ($\lambda_{max,\ film}$). (c) Oxidation potential (E_{ox}) and the corresponded HOMO energy level (E_{HOMO}), and (d) reduction potential (E_{re}) and the corresponded LUMO energy level (E_{LUMO}). (e) Electrochemical bandgap from E_{HOMO} and E_{LUMO} ($E_{g,\ elec}$).

© 2025 Wiley-VCH GmbH

15214095, 2025, 38, Downloaded from https://advanced.onlinelibrary.wiley.com/doi/10.1002/adma.202506449 by Ulsan National Institute Of, Wiley Online Library on [03/12/2025]. See the Terms and Conditions (https://onlinelibrary.wiley.com/terms-and-conditions) on Wiley Online Library for rules of use; OA articles are governed by the applicable Creative Commons License

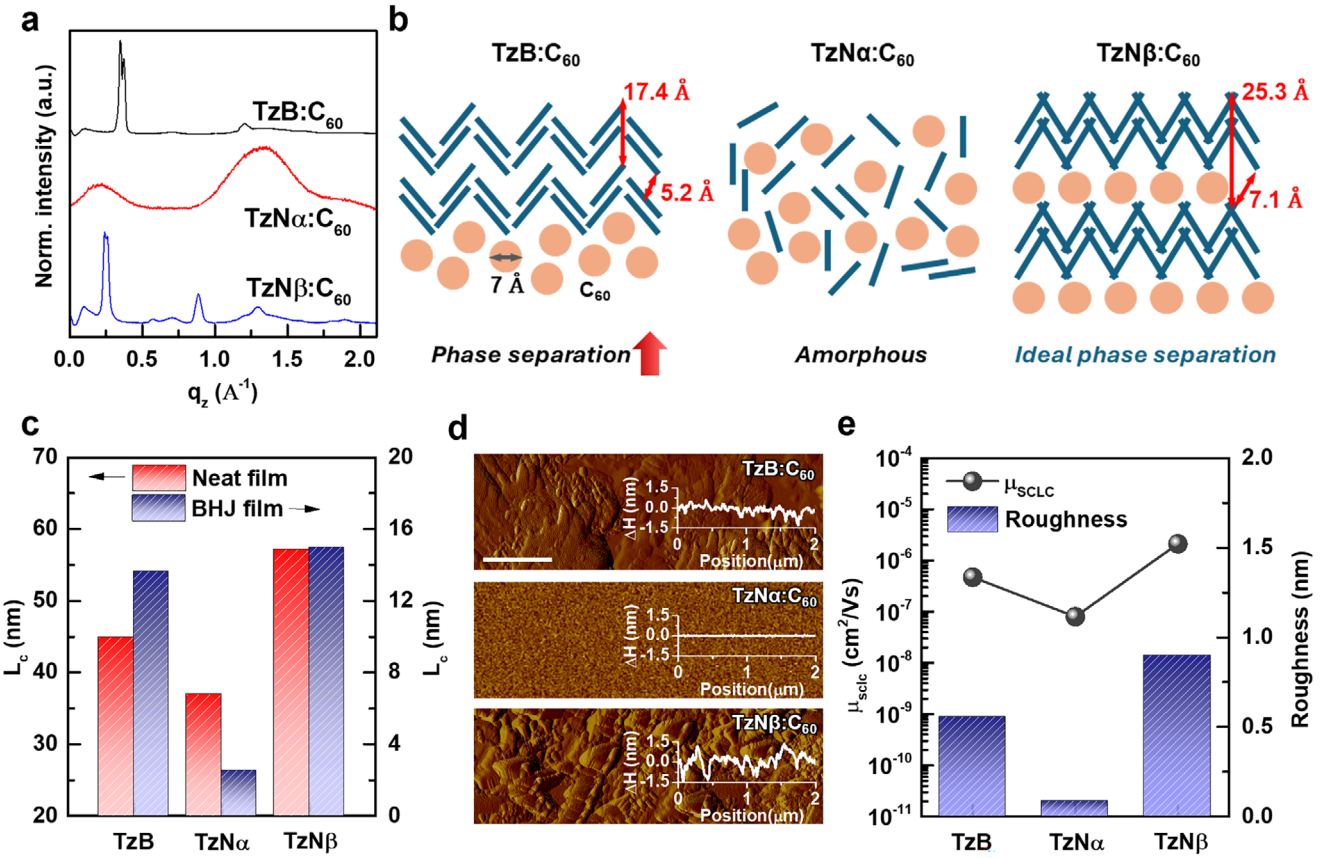

Figure 3. a) Corresponding out-of-plane line-cut profiles of TzB, TzNα, and TzNβ BHJ films, highlighting molecular ordering along the vertical direction. b) Schematic illustration of the estimated crystalline ordering in the BHJ films. c) Calculated coherence lengths along the out-of-plane direction for both neat and BHJ films. d) AFM images of the BHJ films (scale bar: 1 μm). The inset displays the height distribution of the films. e) Comparison of SCLC hole mobility and surface roughness for the three blends.

similar optical and electrochemical properties, their crystallinity varies significantly depending on the planarity of the moiety and strength of π–π interactions. The TzB neat film displayed a partially ordered structure characterized by distinct ring patterns, whereas the TzNα film appeared amorphous. Notably, the TzNβ film exhibited single-crystal-like features with pronounced in-plane ordering, attributed to its optimized dihedral angles and π-extended backbone structure. Summarized parameters are displayed in Table S2 (Supporting Information).

2.2. Thin Film Properties

2D-GIWAXS measurements were also conducted on the BHJ films (Figures S11 and S12, Supporting Information), and the extracted structural parameters are summarized in Table S3 (Supporting Information). The BHJ layers were fabricated by co-evaporating each synthesized small molecule (TzB, TzNα, and TzNβ) with the C_{60} acceptor. C_{60} was selected owing to its high electron transport properties and optical transparency in the visible region. As shown in **Figure 3a**, the TzB:C_{60} and TzNβ:C_{60} blends exhibited distinct (100) crystalline peaks in the out-of-plane (q_z) direction at 0.360 and 0.248 Å^{-1}, corresponding to lamellar d-spacings of ≈17.4 and ≈25.3 Å, respectively. Two overlapping peaks were observed for TzB, indicating a tilted herringbone-type crystalline ordering, consistent with the SCXRD results. In contrast, the TzNα:C_{60} film showed only an azimuthally uniform scattering ring from C_{60} at 0.19 and 1.4 Å^{-1}, indicative of an amorphous morphology. This lack of molecular ordering is attributed to the twisted conformation of TzNα, which hinders sπ–π stacking, whereas the planar, π-extended backbones of TzB and TzNβ facilitate crystallinity in the blend films.

To further understand molecular ordering differences in the blends, the crystalline structure within the BHJ films was estimated based on SCXRD and 2D-GIWAXS results. A schematic summary of the intermolecular packing in the TzB:C_{60}, TzNα:C_{60}, and TzNβ:C_{60} blend films is presented in Figure 3b. First, TzB exhibits high molecular planarity and forms a densely packed structure with a lamellar d-spacing of 17.4 Å with an interplanar distance of 5.2 Å as determined from SCXRD (detailed scheme in Figure S10 (Supporting Information). This compact arrangement makes it difficult for 7 Å-diameter C_{60} molecules to be inserted between the TzB lattices, resulting in a phase-separated morphology. This interpretation is further supported by the 2D-GIWAXS image shown in Figure S11 (Supporting Information), where both the crystalline diffraction peaks of TzB and the amorphous halo of C_{60} are clearly observed,

© 2025 Wiley-VCH GmbH

15214095, 2025, 38, Downloaded from https://advanced.onlinelibrary.wiley.com/doi/10.1002/adma.202506449 by Ulsan National Institute Of, Wiley Online Library on [03/12/2025]. See the Terms and Conditions (https://onlinelibrary.wiley.com/terms-and-conditions) on Wiley Online Library for rules of use; OA articles are governed by the applicable Creative Commons License

indicating the formation of large, well-separated domains for each component. In contrast, in the TzNα:C_{60} blend film, only the amorphous halo pattern of C_{60} is observed, while no crystalline diffraction peaks corresponding to TzNα are detected. This absence of crystallinity is attributed to the twisted molecular conformation of TzNα, which disrupts the intermolecular ordering of TzNα in the blend states. Consequently, this structural disorder likely hinders efficient charge transport within the device, potentially leading to reduced OPD performance.

In the case of TzNβ:C_{60}, the characteristic halo pattern of C_{60} is barely detectable. Instead, a distinct crystalline peak corresponding to a lamellar d-spacing of 25.4 Å is strongly detected with an interplanar distance of 7.1 Å. This result suggests that C_{60} molecules are effectively intercalated into the crystalline lattice of TzNβ without undergoing self-aggregation, thereby forming a well-intermixed bicontinuous nanonetwork. This ideal nanostructure of the co-evaporated TzNβ:C_{60} blend films facilitates efficient charge extraction and transport within the devices, thereby contributing to their excellent OPD performance.

Corresponding coherence lengths (L_c) of neat and BHJ films are calculated using the Scherrer equation and plotted in Figure 3c. Among the molecules, TzNβ exhibited the highest L_c in both neat and BHJ films, reaching 57.17 and 14.96 nm, respectively. Given that a higher L_c facilitates efficient charge transport in organic electronics, TzNβ is considered to exhibit the most favorable morphology among the molecules.

Atomic force microscopy (AFM) images of the three BHJ films (Figure 3d) reveal smooth surface morphologies, with root-mean-square roughness (R_q) values below 1.0 nm for all samples. The roughness increased in the order TzNα:C_{60} < TzB:C_{60} < TzNβ:C_{60}, suggesting that higher crystallinity or localized aggregation leads to increased surface roughness. Notably, as shown in Figure 3e, this trend correlates with the measured space-charge-limited current (SCLC) hole mobilities (Figure S13, Supporting Information). Devices based on TzNβ:C_{60} exhibited the highest mobility of 2.11×10^{-6} cm^2 V^{-1} s^{-1}, followed by TzB:C_{60} (4.71×10^{-7} cm^2 V^{-1} s^{-1}) and TzNα:C_{60} (7.99×10^{-8} cm^2 V^{-1} s^{-1}). These results clearly demonstrate that backbone planarity and molecular ordering play a critical role in enhancing vertical charge transport in the devices.

2.3. OPD Performances

Vacuum-deposited *p–n* bulk heterojunction (BHJ) UV-OPDs were fabricated with an ITO/HAT-CN/TPD/BHJ/C_{60}/Bphen/Al architecture (**Figure** 4a,b), following our previously reported protocol.[33] Full names of molecules used are displayed in Experimental Section. All devices exhibited typical *p–n* junction current density–voltage (*J–V*) characteristics (Figure 4c), but with notable differences in photocurrent density (J_{ph}) and dark current density (J_d). Among them, the TzNα:C_{60} device showed a pronounced increase in J_d under reverse bias, while the TzNβ:C_{60} device maintained a significantly lower dark current. Given that energetic disorder and trap-mediated charge injection are the primary origins of the J_d in BHJ systems,[34,35] the enhanced molecular ordering and dense packing in the TzNβ:C_{60} blend effectively suppressed the thermally activated generation and leakage of current.

The responsivity (R) of the UV-OPDs was calculated using:

$$R = \frac{J_{ph}}{P_{light}} \text{ (A/W)} \quad (1)$$

where J_{ph} is the photocurrent density and P_{light} is the incident light intensity. At –2 V, the R values for TzB:C_{60}, TzNα:C_{60}, and TzNβ:C_{60} devices were 24, 9.0, and 38 mA W^{-1}, respectively. The low R of the TzNα device is attributed to its twisted backbone conformation, while the high R of TzNβ reflects improved charge transport enabled by its planar, π-extended structure.

Specific detectivity (D^*), a key figure of merit for photodetectors, was calculated using:

$$D^* = \frac{R\sqrt{AB}}{i_n} \left(\text{cm Hz}^{0.5}/\text{W or Jones}\right) \quad (2)$$

where A is the active area, B is the bandwidth, and i_n is the noise current. As shown in Figure S14a (Supporting Information), noise current measured at –2 V was 15, 24, and 13 fA Hz$^{-0.5}$ for TzB:C_{60}, TzNα:C_{60}, and TzNβ:C_{60}, respectively—following the same trend as J_d. The resulting D^* values were 4.9×10^{11}, 1.2×10^{12}, and 1.1×10^{12} Jones, with the TzNβ device demonstrating a clear order-of-magnitude improvement. EQE measurements (Figure S14b, Supporting Information) further confirmed this trend, with TzNβ:C_{60} achieving a peak EQE of 27.4% at –5 V, significantly outperforming its counterparts.

Dynamic performance was evaluated by measuring rise/fall times and –3 dB cutoff frequencies (Figure 4e,f). The rise time (t_r) and fall time (t_f)—defined as the time to reach 10–90% and 90–10% of the signal peak—were 15.7/16.4 µs for TzB, 31.6/35.7 µs for TzNα, and 7.6/8.1 µs for TzNβ devices under 5 kHz modulation at –2 V. The TzNβ device exhibited a speed approximately twice that of TzB and 4.5 times that of TzNα. The corresponding –3 dB cutoff frequencies (f_{-3dB}) were 27.7, 19.7, and 50.1 kHz, respectively, with TzNβ:C_{60} again exhibiting the fastest response. To the best of our knowledge, these dynamic parameters are among the highest reported for UV-OPDs. As shown in Figure S14c (Supporting Information), the TzNβ:C_{60} device exhibited the highest stability among the samples stored under ambient conditions, with less than 15% degradation over 120 h.

A summary of key static and dynamic device characteristics is provided in **Table** 2. Among all devices, TzNβ:C_{60} demonstrated superior UV selectivity, responsivity, detectivity, and response speed. These findings clearly establish a strong structure–performance relationship, in which the planar and π-extended TzNβ backbone enhances thermal stability, molecular ordering, vertical charge transport, and high-speed operation in UV-OPDs.

2.4. Integration with CIS

Visible-transparent UV-OPDs based on TzNβ:C_{60} were monolithically integrated onto Si-PDs-based CIS. For successful integration, a transparent top electrode is essential. To this end, a dielectric/metal/dielectric (DMD) electrode structure was employed, with its transmittance characteristics presented in Figure S15 (Supporting Information). The transmittance spectrum of

© 2025 Wiley-VCH GmbH

15214095, 2025, 38, Downloaded from https://advanced.onlinelibrary.wiley.com/doi/10.1002/adma.202506449 by Ulsan National Institute Of, Wiley Online Library on [03/12/2025]. See the Terms and Conditions (https://onlinelibrary.wiley.com/terms-and-conditions) on Wiley Online Library for rules of use; OA articles are governed by the applicable Creative Commons License

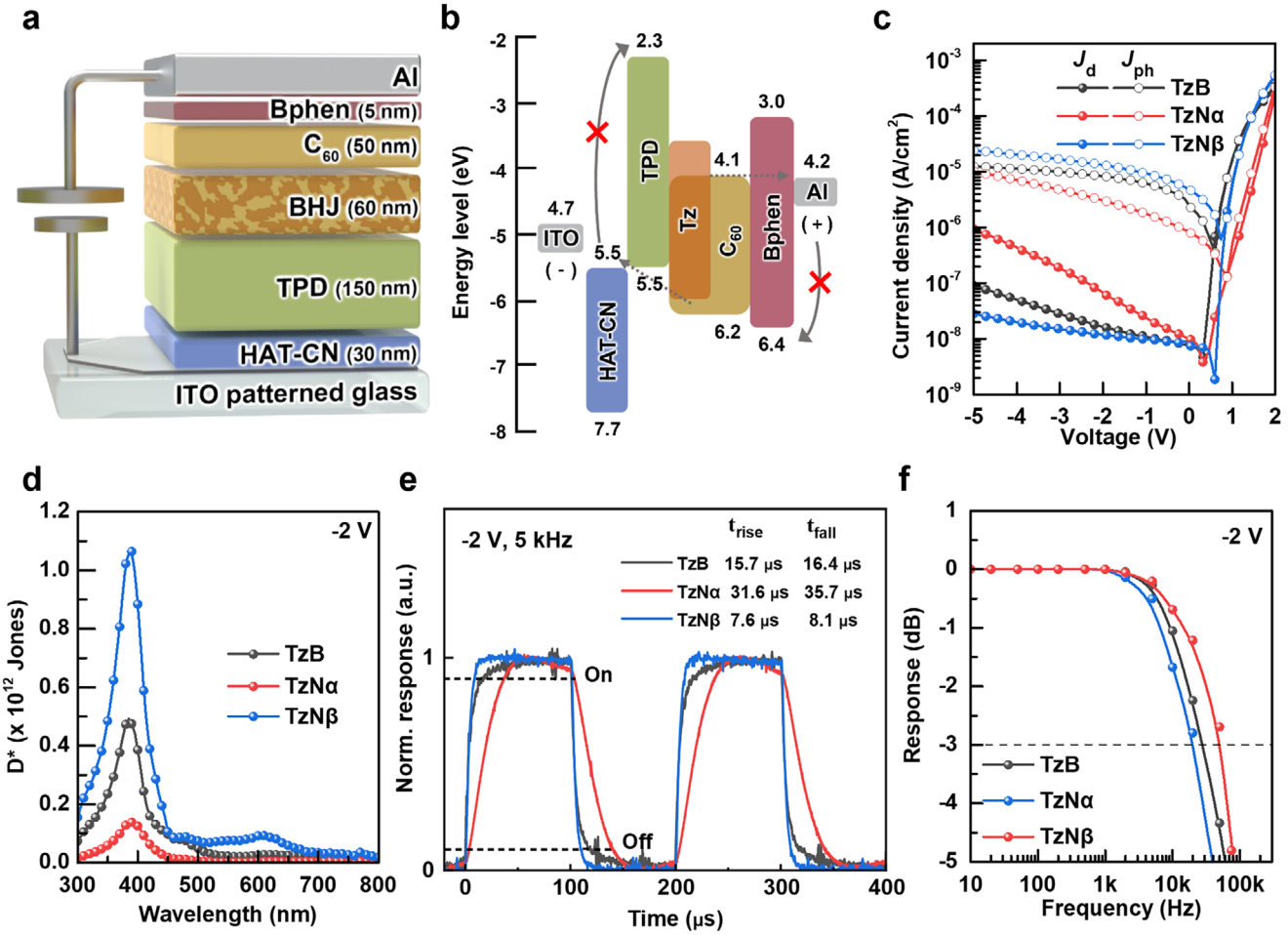

Figure 4. a) Schematic illustration of the UV-OPD device architecture. b) Energy level diagrams of the device components. c) Current density–voltage (*J*–*V*) characteristics under 400 nm illumination at an intensity of 2.72 × 10^{-4} W cm^{-2}. d) Specific detectivity (D^*) as a function of bias voltage. e) Transient photoresponse curves. f) –3 dB cutoff frequencies of TzB:C_{60}, TzNα:C_{60}, and TzNβ:C_{60}-based devices.

the TzNβ:C_{60} UV-OPD is shown in **Figure** 5a, alongside the photopic response of the human eye. The device exhibited high optical transparency, with an average visible transmittance (AVT) of 52.08% (see Experimental Section for calculation details). Peak transmittance occurred in the 500–600 nm range, aligning well with the region of highest visual sensitivity, thereby making the device particularly suitable for integration with commercial CIS. Photographs of the standalone UV-OPD and the integrated CIS are shown in Figure 5b,c, respectively. The full system architecture, including the Si readout integrated circuit (ROIC), is illustrated in Figure 5d. The ROIC consists of a 64 × 120 effective-resolution pixel array based on a four-transistor active pixel sensor (4T-APS) and 3T-APS design, accommodating both visible and UV optical paths.

Importantly, even after UV-OPD integration, the underlying Si-PDs retained their ability to detect visible light, owing to the high transparency of the UV-OPD layer. This is confirmed by the EQE spectra shown in Figure 5e, where the UV-OPDs exhibited peak sensitivity at 380 nm and the Si-PDs at 580 nm. The clear spectral separation allows for simultaneous UV and visible detection without spatial interference, enabling true multifunctional imaging capabilities. To evaluate the UV sensing capabilities in pixel-level, the signal output and pixel-to-pixel variations of the OPDs were measured, as shown in Figure 5f,g. The OPDs

Table 2. UV-OPD properties under a bias of –2 V.

	J_d [A/cm^2]	*R* [mA/W]	EQE [%]	i_n [fA/$Hz^{0.5}$]	D^* [Jones]	f_{-3dB} [Hz]	t_r/t_f [μs]
TzB	1.63 × 10^{-8}	23.5	7.92	15	0.492 × 10^{12}	27,800	15.7/16.4
TzNα	6.63 × 10^{-8}	8.79	2.98	24	0.115 × 10^{12}	19,300	31.6/35.7
TzNβ	1.16 × 10^{-8}	37.5	14.8	13	1.06 × 10^{12}	50,100	7.6/8.1

© 2025 Wiley-VCH GmbH

15214095, 2025, 38, Downloaded from https://advanced.onlinelibrary.wiley.com/doi/10.1002/adma.202506449 by Ulsan National Institute Of, Wiley Online Library on [03/12/2025]. See the Terms and Conditions (https://onlinelibrary.wiley.com/terms-and-conditions) on Wiley Online Library for rules of use; OA articles are governed by the applicable Creative Commons License

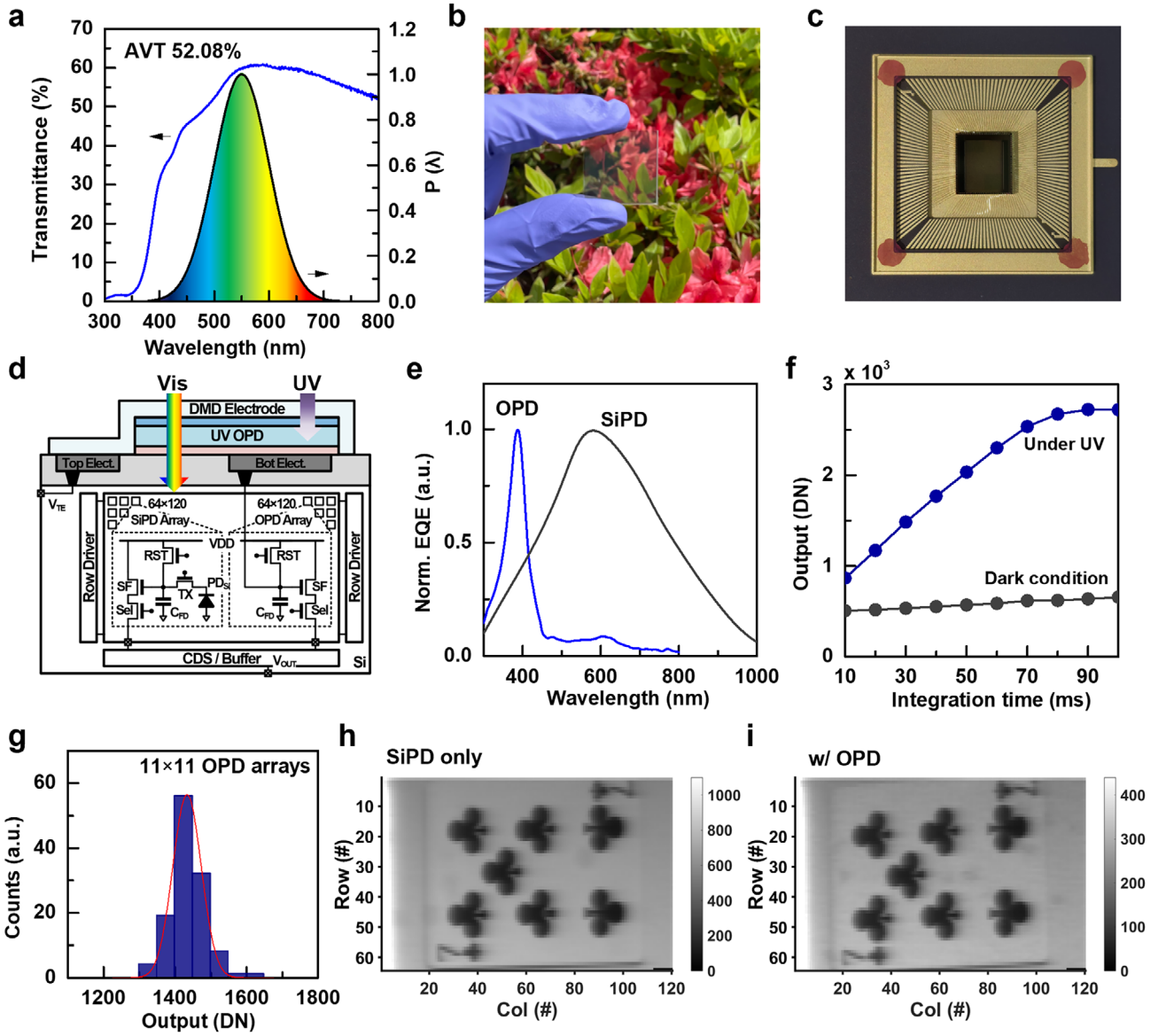

Figure 5. a) Measured transmittance spectrum of the TzNβ:C_{60}-based UV-OPD and normalized photopic response of the human eye. b) Photograph of the fabricated UV-OPD, and c) monolithically integrated CIS. d) Schematic of the integrated CIS architecture including the Si readout circuit. e) Normalized EQE spectra of the UV-OPD and underlying Si-PD, showing distinct spectral separation. f) Output characteristics of the UV-OPDs under dark and illuminated conditions, with mean values obtained from 121 pixels. g) Histogram for UV-OPD pixels including 11 columns and 11 rows (total 121 pixels), with an integration time of 50 ms. h–i) Captured images using (h) the CIS without OPD integration, and (i) the CIS with UV-OPD integration.

exhibited a linear increase in output signal up to the saturation point, suggesting consistent photocurrent generation and reliable readout performance. The mean output and standard deviation of the pixel signals were 1435.4 and 48.56 DN, respectively, corresponding to a coefficient of variation of 3.38%, which demonstrates uniform pixel characteristics across the sensor array.

To assess practical performance, images were captured before and after UV-OPD integration (Figure 5h,i). Although responsivity decreased by ≈50% due to light attenuation through the UV-OPD layer, the processed images remained visually indistinguishable from the original. Histogram standard deviation analysis of a white scene (Figure S17, Supporting Information) showed no significant differences, indicating negligible optical crosstalk or image degradation. These results clearly demonstrate the practical feasibility of monolithic integration of visible-transparent UV-OPDs into conventional CIS platforms, offering enhanced multifunctionality without sacrificing spatial resolution or image quality.

3. Conclusion

In this study, we synthesized and systematically investigated three novel thiazolothiazole (Tz)-based small molecules—TzB,

© 2025 Wiley-VCH GmbH

15214095, 2025, 38, Downloaded from https://advanced.onlinelibrary.wiley.com/doi/10.1002/adma.202506449 by Ulsan National Institute Of, Wiley Online Library on [03/12/2025]. See the Terms and Conditions (https://onlinelibrary.wiley.com/terms-and-conditions) on Wiley Online Library for rules of use; OA articles are governed by the applicable Creative Commons License

TzNα, and TzNβ—as UV-selective active-layer materials for high-performance, vacuum-deposited organic photodiodes (UV-OPDs). These compounds were efficiently prepared via a one-step heterocyclic ring-forming reaction between an aryl aldehyde and dithiooxamide, followed by straightforward purification through recrystallization. We identified π-conjugation length and backbone planarity as key molecular design parameters governing intermolecular ordering and charge transport. Among the three molecules, TzNβ—with its extended conjugation and highly planar backbone—demonstrated the most favorable solid-state properties, including enhanced hole mobility and efficient vertical charge transport. As a result, TzNβ-based UV-OPDs exhibited outstanding performance, achieving a high responsivity of 38 mA W^{-1}, a specific detectivity (D^*) of 1.06×10^{12} Jones, and excellent UV selectivity characterized by a narrow full-width at half-maximum (FWHM) of 60 nm centered at 385 nm. Notably, the devices also demonstrated ultrafast operation, with a –3 dB cutoff frequency of 50.1 kHz—among the highest reported for UV-OPDs to date. These results offer valuable insights into the molecular engineering of π-conjugated small molecules for selective UV detection. Furthermore, the semi-transparent nature of the TzNβ-based UV-OPDs enabled their seamless monolithic integration onto CIS, successfully demonstrating multifunctional imaging capability without compromising spatial resolution or visible-light detection. Taken together, our findings highlight the promise of rational molecular design for advancing UV photodetector technologies and expanding their practical application in next-generation optoelectronic systems.

4. Experimental Section

Synthesis of Materials: Dimethylformamide(DMF) was purchased from Daejung chemicals & materials. Dithiooxamide, Benzaldehyde, 1-Naphthaldehyde and 2-Naphthaldehyde were purchased from Sigma Aldrich. All materials were used without further purification.

Synthesis of TzB (2,5- diphenylthiazolo[5,4-*d*]thiazole). Dithiooxamide (1 g, 8.32 mmol) and benzaldehyde (2.20 g, 20.80 mmol) were dissolved in DMF (20 mL). the reaction mixture was refluxed at 140 °C for 12 h. After the reaction was completed, the mixture was quenched with methanol and poured into cold methanol to precipitate. The crude product was filtered and washed with methanol, and final product was obtained as a yellow solid (2.31 g, 94.5%). ^{1}H NMR (600 MHz, $CDCl_3$) δ 8.03 – 7.99 (m, 2H), 7.51 – 7.47 (m, 3H). MALDI-TOF mass: *m/z* (ESI: 2,5-dihydroxybenzoic acid (2,5-DHB)): 297.24 $[M]^+$.

Synthesis of TzNα (2,5-di(naphthalen-1-yl)thiazolo[5,4-*d*]thiazole). TzNα was synthesized using a procedure similar to that used for TzB. Dithiooxamide (1 g, 8.32 mmol), 1-Naphthaldehyde (3.24 g, 2.80 mmol), and DMF (20 mL) were used to obtain TzNα as a yellow solid (2.70 g, 82.34%). ^{1}H NMR (600 MHz, $CDCl_3$) δ 8.95 (dd, J = 8.6, 1.1 Hz, 1H), 8.01 (d, J = 8.2 Hz, 1H), 7.97 – 7.93 (m, 2H), 7.66 (ddd, J = 8.4, 6.7, 1.4 Hz, 1H), 7.61 – 7.58 (m, 2H). MALDI-TOF mass: *m/z* (ESI: 2,5-dihydroxybenzoic acid (2,5-DHB)): 398.24 $[M]^+$.

Synthesis of TzNβß (2,5-di(naphthalen-2-yl)thiazolo[5,4-*d*]thiazole). TzNβ was synthesized using a procedure similar to that used for TzB. Dithiooxamide (1 g, 8.32 mmol), 2-Naphthaldehyde (3.24 g, 20.80 mmol), and DMF (20 mL) were used to obtain TzNβ as a yellow solid (2.58 g, 78.66%). ^{1}H NMR (600 MHz, $CDCl_3$) δ 8.50 (d, J = 1.8 Hz, 1H), 8.13 (dd, J = 8.5, 1.8 Hz, 1H), 7.97 – 7.94 (m, 2H), 7.90 – 7.87 (m, 1H), 7.58 – 7.55 (m, 2H). MALDI-TOF mass: *m/z* (ESI: 2,5-dihydroxybenzoic acid (2,5-DHB)): 396.87 $[M]^+$.

Material Characterization: A VARIAN 600 MHz Spectrometer was used to measure the ^{1}H spectra of all organic compounds. The absorption spectra were obtained on a JASCO V-730 UV/VIS absorption spectrometer. Cyclic voltammetry (CV) measurement was carried out using WonA tech ZIVE SP1(1A) with the three-electrode cell and Ag/Ag^+ reference electrode, solution of 0.1 M tetrabutylammonium hexafluorophosphate (Bu_4NBF_6) in acetonitrile (CH_3CN) as the electrolyte, the working electrode was coated with organic materials by dipping into organic materials in chloroform. The electrochemical potential of the materials was calculated with respect to the ionization potential of ferrocene/ferrocenium ion(Fc/Fc^+) as an internal standard, −4.8 eV.

DFT calculations were performed using the Gaussian 16W software package. The geometrical optimization of the dimeric structures was performed using Becke's three-parameter exchange functional in combination with the Lee-Yang-Parr correlation functional (B3LYP) and the 6–31G(d,p) basis set.

Single-crystal X-ray diffraction (SCXRD) measurements were carried out using a Bruker D8 QUEST ECO diffractometer equipped with a Mo Kα radiation source (λ = 0.71073 Å) and a Photon II 7 area detector (active area: 70 × 100 mm^2, max count rate: 500,000 CPS). The instrument features a microfocus X-ray generator (max 50 kV, 25 mA, 1 kW) and a point focus Mo X-ray tube. Data collection was performed at 25 °C using a KAPPA APEX sample stage, with phi rotation accuracy of 0.025° and reproducibility of 0.001°. A single crystal suitable for SCXRD analysis was obtained by slow evaporation from methanol. The collected structural data were analyzed using Mercury software.

The thermal stability of the synthesized materials was observed using a Netzsch STA 449F3 at a scanning rate of 10 °C min^{-1} in an N_2 atmosphere, with measurements conducted up to a final temperature of 600°C.

Device Transparency Evaluation: To determine the AVT, the spectral transmittance of the device, T(λ), is combined through integration with the photon flux of the light source, S(λ) — typically the AM 1.5G spectrum — and the photopic response, P(λ). The integrated value is subsequently normalized by the sum of S(λ) and P(λ), as shown in Equation (3).

$$AVT = \frac{\int T(\lambda) \cdot P(\lambda) \cdot S(\lambda)\, d(\lambda)}{\int P(\lambda) \cdot S(\lambda)\, d(\lambda)} \quad (1 \text{ or } \%) \tag{3}$$

The specific wavelength range considered in the AVT calculation depends on the definition of the photopic response, P(λ). In this study, the AVT of the TzNβ:C_{60} devices is determined within the wavelength range of 380–780 nm.

Device Fabrication: We selected the transport layers with reference to previously reported studies on OPD materials.[30] HAT-CN (Hexaazatriphenylenehexacarbonitrile) was purchased from Ossila. TPD (N,N′-Bis(3-methylphenyl)-N,N′-diphenylbenzidine), C_{60}, Bphen (Bathophenanthroline) were purchased from Sigma Aldrich. The molecules were used without further purification.

The ITO-patterned glass substrates were cleaned by sequential ultrasonic treatment in Mucasol solution, deionized water, acetone, and isopropyl alcohol for 15 min each. The substrates were then dried under a flow of N_2 gas. The organic thin films were thermally deposited using a high-vacuum evaporator (≈5×10^{-6} Torr) in a sequential manner. The deposition rate was maintained at 0.02–0.03 nm s^{-1} throughout. The photoactive area of the OPD was 0.09 cm^2.

Device Characterization: *J–V* characteristics and EQE spectra were measured utilizing a Keithley 2450 SourceMeter Unit (SMU) and a 330 W Xe arc lamp with an Oriel Cornerstone 130 1/8 m monochromator. Measurements were controlled with home–made LabView programs. Noise current density spectrum was obtained using Stanford Research SR830 current pre–amplifier and Agilent 35670A spectrum analyzer. Cut-off frequency of the devices was measured with 405 nm laser diode and modulated by a function generator, pre–amplifier and digital oscilloscope (Tektronix 4 series B MSO). Hole-only devices (ITO/HAT-CN/TPD/BHJ/MoO_3/Ag) were measured under dark conditions to evaluate their hole mobilities.

Film Characterization: The 2D-GIWAXS measurements of the pristine and BHJ films of the organic materials were performed with with a high-resolution synchrotron X-ray beam source, located at the 3C beamline of the Pohang Accelerator Laboratory (Republic of Korea), with a grazing

© 2025 Wiley-VCH GmbH

15214095, 2025, 38, Downloaded from https://advanced.onlinelibrary.wiley.com/doi/10.1002/adma.202506449 by Ulsan National Institute Of, Wiley Online Library on [03/12/2025]. See the Terms and Conditions (https://onlinelibrary.wiley.com/terms-and-conditions) on Wiley Online Library for rules of use; OA articles are governed by the applicable Creative Commons License

incidence angle of ≈0.16° under low-vacuum conditions. AFM (Park systems, NX10) was used to observe the surface morphology and film roughness. The film thickness was set to 60 nm for all conditions, consistent with the configuration used in the OPDs.

Imaging Characterization and Demonstration: For the imaging characterization and demonstration, integrated chip was wirebonded and packaged by 144PGA cavity. Test printed circuit board (PCB) was designed with commercial ICs and passive components. AD8641 and AD9235 were used for analog-to-digital converting. OPD pixels with an 8.1 µm pitch and a top-metal-opening architecture were designed. Cmount and MV0813 lens are adopted for focusing the image to the sensor. Throughout the test, Integration time was 50ms with the anlaog gain of 4 by CDS block. Commercial LED was illuminated to the target for the image demonstration. 100 frames were averaged for the depicted image. EQE of Si-PDs are measured using tunable light source consist of power supply (OPS-Q250), lamp source (Newport-66884), monochromator (Newport-90078702-SI), integrated sphere, power meter (Newport-1936-R), and halogen lamp (Newport, 6335 Quartz Tungsten Lamp, 252 W).

Supporting Information

Supporting Information is available from the Wiley Online Library or from the author.

Acknowledgements

J.P. and W.J.P. contributed equally to this work. This research was supported by Nanomaterial Technology Development Program through the National Research Foundation of Korea (NRF) funded by Ministry of Science and ICT, South Korea (2022M3H4A1A03067131), and also supported by the Technology Innovation Program (RS-2024-00422305, Development of deposition-type highly heat-resistant Near-infrared emitting/absorbing organic materials and de-vice for implementation of all-in one sensor OLED display) funded by the Ministry of Trade, Industry and Energy (MOTIE, Korea).

Conflict of Interest

The authors declare no conflict of interest.

Data Availability Statement

The experimental data that supports the findings of this study are available from the corresponding author upon reasonable request.

Keywords

CMOS image sensors, organic photodiodes, small molecules, UV-selective photodiodes

Received: April 4, 2025
Revised: June 16, 2025
Published online: July 7, 2025

[1] Z. Li, T. Yan, X. Fang, *Nat. Rev. Mater.* **2023**, *8*, 587.
[2] X. Li, Z. Li, J. Hu, B. Huang, J. Shi, Z. Zhong, Y. Zhuang, Y. Chen, J. Wang, J. Li, L. Zhang, X. Meng, W. Shi, S. Chen, X. Fang, H. Huang, J. Wang, J. Chu, *Nat. Commun.* **2025**, *16*, 2209.
[3] V. Slavinsky, J. Helmy, J. Vroman, M. Valdebran, *International Journal of Dermatology* **2024**, *63*, 288.
[4] A. Verma, A. Zanoletti, K. Y. Kareem, B. Adelodun, P. Kumar, F. O. Ajibade, L. F. O. Silva, A. J. Phillips, T. Kartheeswaran, E. Bontempi, A. Dwivedi, *Environ. Chem. Lett.* **2024**, *22*, 273.
[5] M. M. Delorme, J. T. Guimarães, N. M. Coutinho, C. F. Balthazar, R. S. Rocha, R. Silva, L. P. Margalho, T. C. Pimentel, M. C. Silva, M. Q. Freitas, D. Granato, A. S. Sant'Ana, M. C. K. H. Duart, A. G. Cruz, *Trends Food Sci. Technol.* **2020**, *102*, 146.
[6] J. Staehelin, N. R. P. Harris, C. Appenzeller, J. Eberhard, *Reviews of Geophysics* **2001**, *39*, 231.
[7] J. F. Bornman, P. W. Barnes, S. A. Robinson, C. L. Ballaré, S. D. Flint, M. M. Caldwell, *Photochem. Photobiol. Sci.* **2015**, *14*, 88.
[8] J. Ferrand, J. Dabin, O. Chevallier, M. Kane-Charvin, A. Kupai, J. Hrit, S. B. Rothbart, S. E. Polo, *Nat. Commun.* **2025**, *16*, 746.
[9] A. De Magis, M. Limmer, V. Mudiyam, D. Monchaud, S. Juranek, K. Paeschke, *Nat. Commun.* **2023**, *14*, 6705.
[10] Z.-X. Liang, Y.-Y. Zhao, J.-T. Chen, X.-Z. Dong, F. Jin, M.-L. Zheng, X.-M. Duan, *Nat. Commun.* **2025**, *16*, 2086.
[11] S. Xue, Z. Shi, Z. Wang, H. Tan, F. Gao, Z. Zhang, Z. Ye, S. Nian, T. Han, J. Zhang, Z. Zhao, B. Z. Tang, Q. Zhang, *Nat. Commun.* **2024**, *15*, 10084.
[12] J. Tao, D. Liu, Z. Qin, B. Shao, J. Jing, H. Li, H. Dong, B. Xu, W. Tian, *Adv. Mater.* **2020**, *32*, 1907791.
[13] R. D. Jansen-van Vuuren, A. Armin, A. K. Pandey, P. L. Burn, P. Meredith, *Adv. Mater.* **2016**, *28*, 4766.
[14] Y. Lim, S. Yun, D. Minami, T. Choi, H. Choi, J. Shin, C.-J. Heo, D.-S. Leem, T. Yagi, K.-B. Park, S. Kim, *ACS Appl. Mater. Interfaces* **2020**, *12*, 51688.
[15] X. Bulliard, Y. W. Jin, G. H. Lee, S. Yun, D.-S. Leem, T. Ro, K.-B. Park, C.-J. Heo, R.-I. Satoh, T. Yagi, Y. S. Choi, S.-J. Lim, S. Lee, *J. Mater. Chem. C* **2016**, *4*, 1117.
[16] G. H. Lee, X. Bulliard, S. Yun, D.-S. Leem, K.-B. Park, K.-H. Lee, C.-J. Heo, I.-S. Jung, J.-H. Kim, Y. S. Choi, S.-J. Lim, Y. W. Jin, *Opt. Express* **2019**, *27*, 25410.
[17] S. Park, Y. Lim, C.-J. Heo, S. Yun, D.-S. Leem, S. Kim, B. Choi, K.-B. Park, *Optica* **2022**, *9*, 992.
[18] S. Cai, X. Xu, W. Yang, J. Chen, X. Fang, *Adv. Mater.* **2019**, *31*, 1808138.
[19] Y. Ma, Q. Gao, Y. Li, Y. Du, Y. Huang, Y. Sun, X. Chen, W. Wu, F. Wu, Z. Wang, L. Zhao, Y. Hu, C. Han, L. Li, C. Yang, W. Hu, *Adv. Mater.* **2025**, *37*, 2414589.
[20] M. R. Esopi, M. Calcagno, Q. Yu, *Adv. Mater. Technol.* **2017**, *2*, 1700025.
[21] D. Guo, L. Yang, J. Zhao, J. Li, G. He, D. Yang, L. Wang, A. Vadim, D. Ma, *Mater. Horiz.* **2021**, *8*, 2293.
[22] I. H. Jung, J. Yu, E. Jeong, J. Kim, S. Kwon, H. Kong, K. Lee, H. Y. Woo, H.-K. Shim, *Chemistry – A European Journal* **2010**, *16*, 3743.
[23] J. R. Johnson, R. Ketcham, *J. Am. Chem. Soc.* **1960**, *82*, 2719.
[24] I. Osaka, G. Sauvé, R. Zhang, T. Kowalewski, R. D. McCullough, *Adv. Mater.* **2007**, *19*, 4160.
[25] L. Zhou, L. Meng, J. Zhang, S. Qin, J. Zhang, X. Li, J. Li, Z. Wei, Y. Li, *Adv. Sci.* **2022**, *9*, 2203513.
[26] S. Halder, A. K. Pradhan, P. Sivasakthi, P. K. Samanta, C. Chakraborty, *Materials Today Chemistry* **2023**, *34*, 101768.
[27] J. Wu, F. Sun, F. Hua, W. Hou, X. Xia, X. Guo, D. Yu, E. Wang, Y. Li, M. Zhang, *Adv. Energy Mater.* **2025**, *15*, 2500024.
[28] Y. Feng, X. Qiao, G. Ouyang, G. Liu, H. Li, *Adv. Electron. Mater.* **2020**, *6*, 1901443.
[29] J. Wu, G. Li, J. Fang, X. Guo, L. Zhu, B. Guo, Y. Wang, G. Zhang, L. Arunagiri, F. Liu, H. Yan, M. Zhang, Y. Li, *Nat. Commun.* **2020**, *11*, 4612.
[30] C. So, W. J. Pyo, D. S. Chung, *Adv. Photonics Res.* **2025**, *6*, 2400094.

© 2025 Wiley-VCH GmbH

15214095, 2025, 38, Downloaded from https://advanced.onlinelibrary.wiley.com/doi/10.1002/adma.202506449 by Ulsan National Institute Of, Wiley Online Library on [03/12/2025]. See the Terms and Conditions (https://onlinelibrary.wiley.com/terms-and-conditions) on Wiley Online Library for rules of use; OA articles are governed by the applicable Creative Commons License

[31] S. S. Dharmapurikar, S. Chithiravel, M. V. Mane, G. Deshmukh, K. Krishnamoorthy, *Chem. Phys. Lett.* **2018**, *695*, 51.
[32] F. Garnier, G. Horowitz, X. Z. Peng, D. Fichou, *Synth. Met.* **1991**, *45*, 163.
[33] W. J. Pyo, G. Kim, S. Kim, H. Oh, D. Keum, B. Kim, D. Kim, C. So, S. Lee, D.-W. Jee, I. H. Jung, D. S. Chung, *ACS Nano* **2024**, *18*, 17075.
[34] T. H. Kim, J. H. Lee, M. H. Jang, G. M. Lee, E. S. Shim, S. Oh, M. A. Saeed, M. J. Lee, B.-S. Yu, D. K. Hwang, C. W. Park, S. Y. Lee, J. W. Jo, J. W. Shim, *Adv. Mater.* **2024**, *36*, 2403647.
[35] G. Simone, M. J. Dyson, C. H. L. Weijtens, S. C. J. Meskers, R. Coehoorn, R. A. J. Janssen, G. H. Gelinck, *Adv. Opt. Mater.* **2020**, *8*, 1901568.

 © 2025 Wiley-VCH GmbH

15214095, 2025, 38, Downloaded from https://advanced.onlinelibrary.wiley.com/doi/10.1002/adma.202506449 by Ulsan National Institute Of, Wiley Online Library on [03/12/2025]. See the Terms and Conditions (https://onlinelibrary.wiley.com/terms-and-conditions) on Wiley Online Library for rules of use; OA articles are governed by the applicable Creative Commons License